

X-ray powder diffraction from carbon nanotubes and nanoparticles

D. Reznik

Materials Science and Engineering Laboratory, National Institute of Standards and Technology, Gaithersburg, Maryland 20899

C. H. Olk

Physics Department, General Motors Research & Development Center, Warren, Michigan 48090

D. A. Neumann and J. R. D. Copley

Materials Science and Engineering Laboratory, National Institute of Standards and Technology, Gaithersburg, Maryland 20899

(Received 28 September 1994)

We report detailed x-ray powder-diffraction measurements on a sample consisting of $\sim 60\%$ carbon nanotubes and $\sim 40\%$ carbon nanoparticles. These measurements demonstrate the existence of short-range interlayer stacking correlations. Our calculations show that such correlations should not be observable in idealized models of nanotubes. The observation of short-range interlayer correlations can be explained if many of the nanotubes and nanoparticles have polygonal cross sections, largely consisting of flat regions having graphitic interlayer correlations. This polygonization is almost certainly driven by the van der Waals interactions responsible for the *ABAB* stacking in crystalline graphite.

I. INTRODUCTION

Carbon nanotubes¹ and nanoparticles² may be formed when an arc is struck between graphite electrodes in an inert atmosphere. Transmission electron microscopy (TEM) shows that nanotubes are long hollow cylinders with inner diameters of ~ 25 Å. Single-wall³ as well as multiwall¹ tubes have been observed, some of them displaying fullerene-like caps on the ends.⁴ According to the accepted "Russian doll" model, nanotubes consist of graphite layers rolled up into closed concentric cylinders [Fig. 1(a)].¹ Zhou *et al.*⁵ found that the radial compressibility of a nanotube/nanoparticle mixture is comparable with the *c*-axis compressibility of graphite and that nanotubes can be intercalated with Rb and K. These properties are not expected of Russian doll nanotubes, but they are consistent⁵ with the so-called "scroll" model [Fig. 1(b)], in which a single graphite sheet, possibly containing dislocation defects, is rolled up to form a multiwalled tube.

Each of the cylinders in Russian doll nanotubes is formed from a graphitic sheet that is rolled so that one of its Bravais lattice vectors maps on the circumference of the cylinder.^{6,7} Thus it is possible to start from any point on a cylinder and then, through a succession of lattice vector translations, to return to the same point having gone once around the cylinder. It follows that the radius of any given cylinder may be written as $R_{mn} = (1/2\pi)[(na)^2 + (mb)^2]^{1/2}$ where *m* and *n* are integers, $a = 2.455$ Å is the in-plane graphite lattice constant, and $b = \sqrt{3}a$.

The helical angle of a graphite cylinder may be defined as the smallest angle that any of its C-C bonds makes with a plane normal to the cylinder axis. Thus the helical angle of a Russian doll cylinder is given^{6,8} by $\theta = \arctan(na/mb)$, modulo 60° . It is clear from Fig. 2 that tubes with $\theta = 0^\circ$ or $\theta = 30^\circ$ are special, since in these

cases $\frac{1}{3}$ of the C-C bonds are either perpendicular ($\theta = 0^\circ$) or parallel ($\theta = 30^\circ$) to the cylinder axis, resulting in a repeat period along the tube axis of *a* or *b*, respectively; we shall refer to such tubes as nonhelical tubes. Nanotubes with other values of θ have all C-C bonds at angles other than 0° or 90° to the cylinder axis, and the repeat period is typically much larger than the graphite unit-cell size;⁶ we shall call them helical tubes.

Russian doll and scroll nanotubes can be nonhelical or helical. With few exceptions, it is impossible to construct helical Russian doll nanotubes that maintain the same helical angle from layer to layer with an interlayer spacing d_c reasonably close to that of disordered graphite. Thus the generally accepted picture of helical Russian doll nanotubes is that θ changes from layer to layer so as to maintain the interlayer spacing close to that of disordered graphite. In scroll nanotubes d_c is unrelated to θ , but θ must be the same for all layers (here meaning winds of the spiral), unless there are dislocations.

Nanoparticles are assumed to have an onionlike structure, i.e., to be composed of large concentric fullerene-like

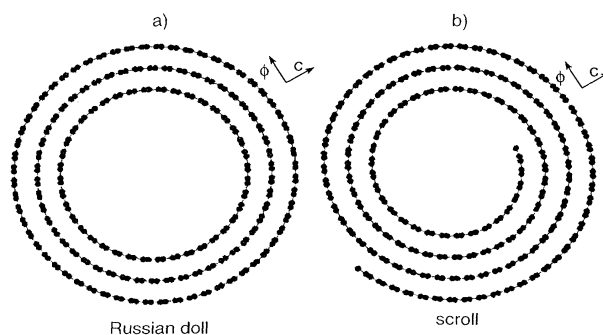


FIG. 1. Top views of (a) Russian doll and (b) scroll multilayer nanotubes. Local *c* and ϕ directions are indicated.

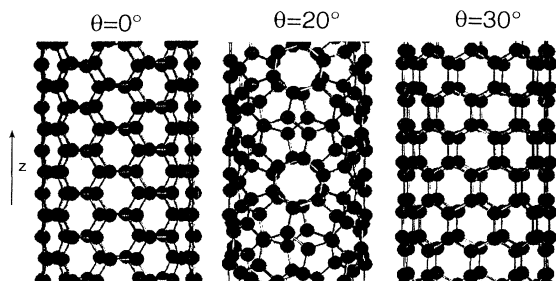


FIG. 2. Side views of single wall nanotubes with different helical angles θ ; $\theta=0^\circ$ and $\theta=30^\circ$ tubes are the only two distinct nonhelical structures.

cages of carbon atoms.² In such structures, each “layer” must contain 12 pentagons in order for the structure to close.

X-ray diffraction is an effective technique to study the average structural properties of carbon nanotube/nanoparticle samples. We present here a detailed analysis of measured x-ray-diffraction patterns for such a sample. The analysis yields important information about structural properties such as tube topology, interlayer correlations, strains, and domain sizes. We also describe calculations of powder x-ray-diffraction patterns for the Russian doll and scroll models of nanotubes described above. A comparison of the calculations with our data reveals that these idealized models are oversimplified and suggests that there are correlated flat graphitic regions in carbon nanomaterial.

II. EXPERIMENTAL DETAILS

Samples were grown by the arc discharge method.⁹ In each case the cathode was a pressed graphite rod 6 mm in diameter, and the 4 mm diameter anode was a composite of graphite and silicon. The anode had a 1 mm diameter hole ~ 10 mm deep drilled in its center and packed with -325 mesh 99.5% pure silicon powder. Energy-dispersive x-ray analysis produced no evidence that Si had been incorporated chemically or in elementary form within the growth. The electrodes were adjusted so that their surfaces were nearly parallel and ~ 1 mm apart. The chamber was evacuated to a pressure of $\sim 10^{-7}$ torr, pumped for several hours, and then backfilled with 99.999% pure helium to an initial pressure of 500 torr. A Miller XMT200 dc inverter was used as the plasma power source. The high breakdown voltage necessary to initiate the plasma was supplied by a separate high-frequency arc starter. While an arc was struck between the electrodes the anode was slowly fed into the plasma using a linear motion mechanism. Nanotubes and nanoparticles formed at the center of the cathode.

Transmission electron micrographs were obtained using a Phillips EM430 operating at 300 kV. Specimens were prepared by scraping material from the cores of the cathodes onto holey, carbon formvar coated, copper TEM grids. This technique produced an ample abundance of nanotubes and nanoparticles that hung over holes in the formvar coating, facilitating examination in the TEM.

A low-resolution TEM image of one of our samples is shown in Fig. 3. About 60% of the sample consists of long nanotubes with an average outer diameter of ~ 400 Å and the rest is polyhedral nanoparticles. No amorphous carbon, which is known to contaminate some nanotube/nanoparticle samples, was observed.

The diffraction measurements were performed with a Scintag XDS2000 x-ray powder-diffractometer using a Cu $K\alpha$ tube and a wavelength λ of 1.54 Å. The beam width at the sample was ~ 0.4 mm. The powder sample was placed in a glass tube with very thin walls (< 0.1 mm). The diffraction pattern of the empty tube was subtracted from the data. Slits of 0.3 mm before the sample, and 0.1 mm after the sample, were used in all the measurements, except for the measurement shown in the inset of Fig. 4, where 0.2/0.05 mm slits were used. Resolution, extracted from the widths of Al_2O_3 Bragg reflections measured under identical experimental conditions, was included in our fits to the experimental data.

III. EXPERIMENTAL RESULTS AND COMPARISON WITH A MODEL OF DISORDERED GRAPHITE

The measured powder-diffraction pattern for the nanotube/nanoparticle sample, plotted as a function of the wave-vector transfer $Q = (4\pi/\lambda)\sin(\alpha/2)$, where α is the scattering angle, is shown in Fig. 4. In agreement with other measurements,^{5,10} it is similar to that of disordered graphite. The main features are sharp, symmetric $00l$ peaks which probe the interlayer spacing, and



FIG. 3. Low resolution TEM photograph of a part of the sample used in our measurements. The area shown is approximately $36 \times 46 \mu\text{m}^2$.

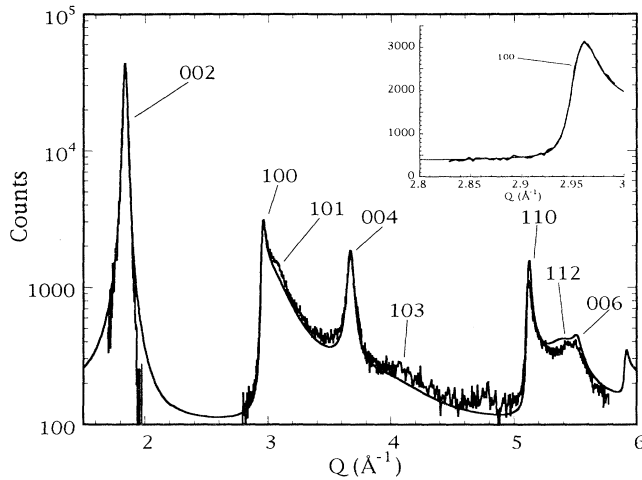


FIG. 4. The measured x-ray powder-diffraction pattern of the nanotube/nanoparticle sample (noisy curve) and the results of a calculation using the model of disordered graphite described in the text (smooth curve). The inset shows the result of a high-resolution measurement around the maximum of the 10 reflection, with the same calculation. The contribution from the sample holder, which is flat, has not been subtracted from the data shown in the inset.

sawtooth-shaped reflections associated with the two-dimensional periodicity of the layers.^{5,10}

Structural information is contained in the shape of the observed scattering, rather than simply in the positions and intensities of the peaks.¹¹ Therefore an important observation is that the widths of the 002 and 004 peaks are not resolution limited. For carbon nanotubes and nanoparticles, there are two likely sources of the observed broadening. One possibility is particle size broadening, which should definitely be observed since TEM shows that the tubes have an average radius of ~ 200 Å. Another possible source, often overlooked, is strain-broadening resulting from a distribution of d spacings which varies more slowly than $1/r^2$.¹² These sources of broadening can be distinguished because they have different dependences of peak width on Q . For the case of domain size broadening, the full width at half maximum (FWHM) is

$$\gamma_f = 2(\pi \ln 2)^{1/2} / Nd_c, \quad (1)$$

where N is the number of layers. Note that γ_f is independent of the order of the reflection. On the other hand, the width for strain broadening is given by

$$\gamma_d = \frac{\pi l}{d_c^2} \Delta(d_c), \quad (2)$$

where l is the index of the reflection and $\Delta(d_c)$ is the FWHM of the distribution of interlayer spacings. Here the width depends linearly on the order of the reflection.

We have separated these contributions by fitting the 002 and 004 peaks to convolutions of Lorentzian and Gaussian line shapes (Fig. 5). The measured resolution function is Gaussian and we assume that the particle size broadening is also Gaussian. The width of the fitted

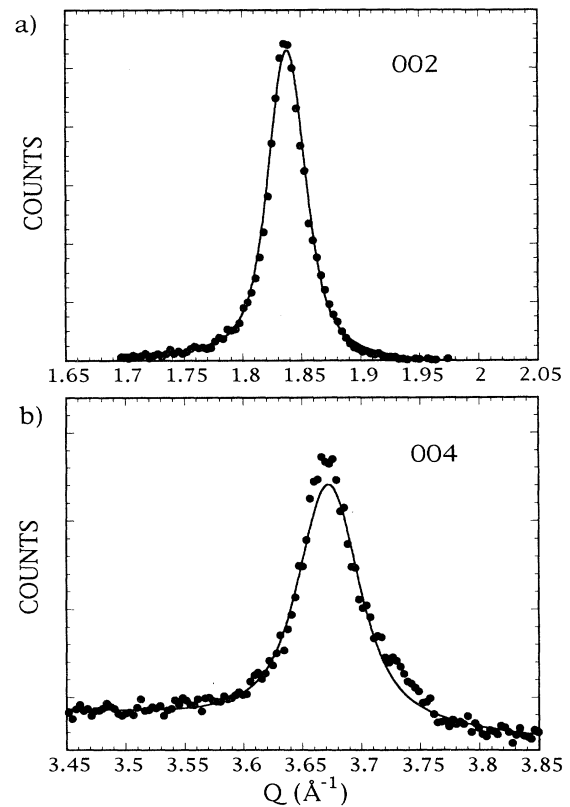


FIG. 5. 00 l peaks fitted to the line shape described in the text (a) 002 peak. (b) 004 peak.

Gaussian component is the quadrature sum of the widths of these two contributions. The Lorentzian component of the 00 l peaks results from the distribution of interlayer spacings. With these assumptions we obtain $N \sim 55$ (which gives $R \sim 190$ Å, consistent with estimates based on an inspection of our TEM results), and $\Delta(d_c) = 0.044$ Å. Thus much of the width of the 00 l peaks arises from strain rather than finite-size effects. If we had assumed that the width of the 002 peak was (apart from resolution) due solely to particle size effects, we would have obtained $N \sim 17$. Figure 6 shows the calculated distribution of d spacings in our sample. It has a maximum at 3.42 Å, slightly lower than the previously reported value of 3.44 Å.^{5,10} The tails of the distribution, which extend from less than 3.354 Å (the ordered graphite spacing) to more than 3.5 Å, are only roughly represented by Fig. 6, since the assumption of a Lorentzian d_c distribution is artificial far from the maximum. This cannot have a large effect on the extracted values of N and $\Delta(d_c)$, but would tend to reduce the extent of the tails in Fig. 6.

While a great deal of information can be obtained from the 00 l peaks, it is impossible to learn anything about the interlayer stacking since this involves in-plane correlations of the graphite layers and Q has no in-plane component for 00 l peaks. In order to obtain information about the interlayer stacking correlations we must look at hkl peaks where h and/or k is nonzero. In crystalline graphite the stacking sequence is $ABAB$ resulting in sharp hkl peaks. On the other hand, if the graphite

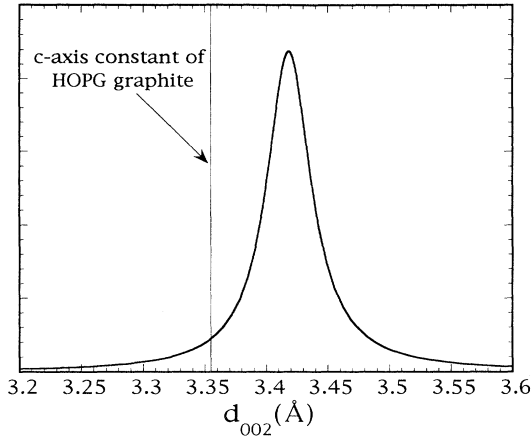


FIG. 6. The calculated distribution of interlayer spacings in our sample. The vertical line is at 3.354 Å—the interlayer spacing in ordered graphite.

sheets are stacked turbostratically the hkl reflections smear into uniform rods perpendicular to the plane of the layers, indexed using only two indices hk . If the sample is polycrystalline, these rods manifest themselves as asymmetric peaks with sharp onsets on the low Q side and broad tails on the high Q side as recognized by Warren.¹³ The broad bumps that we observe in the high Q tails (Fig. 4), centered at the hkl powder peak positions of ordered graphite, represent intensity modulations along the hk rods reflecting a tendency for adjacent layers to be aligned as in ordered graphite.^{14,15} Intensity modulations are also evident in the diffraction pattern published in Ref. 10, but they were not explicitly mentioned in that paper.

Because the diffraction data shown in Fig. 4 look very similar to those expected for disordered graphite with interlayer correlations,¹⁴ we have fitted our data using the formalism for disordered graphite developed in Refs. 14–16. Within this model the diffracted intensity of an hk reflection is proportional to¹⁶

$$I_{hk}(Q) = AC(Q)f^2(Q) \left[1 + \cos \left[\frac{2}{3}\pi(h-k) \right] \right] \times \int_0^{\pi/2} d\Psi \frac{\pi}{2} \cos\Psi I_c(Q \cos\Psi) F(Q \sin\Psi), \quad (3)$$

where Ψ is the angle between Q and the c direction,

$$A = \frac{\pi}{2(Qq_0)^{1/2}[(\gamma\pi/\ln 2)^{1/2} + 1.8\gamma\pi]}$$

is the normalization factor, $C(Q)$ is the polarization factor, $f(Q)$ is the atomic scattering factor for carbon,

$$I_c(x) = e^{-(x-q_0)^2(\ln 2/\gamma^2)} + \frac{1.8\gamma^2}{\gamma^2 + (x-q_0)^2}$$

is the intensity distribution across the rod (see Ref. 16), and

$$F(x) = 1 + \frac{2s}{1-s} + \frac{2}{N} \frac{s^{N+1}-s}{(1-s)^2}$$

is the intensity distribution along the rod with

$$s = e^{ixd_c} \int_{\text{unit cell}} P(\mathbf{r}) e^{iq_0 \cdot \mathbf{r}} d\mathbf{r}$$

(Refs. 14 and 15). In these equations q_0 is the two-dimensional reciprocal-lattice vector for the hk reflection, γ is the width of the reciprocal-lattice rod given by $1/\gamma = D\pi^{-1/2}$ where D is the characteristic domain size of the layers, and $P(\mathbf{r})$ is the probability that the in-plane component of the separation of a pair of adjacent layers is \mathbf{r} . This function is determined by the model of the stacking of the graphite layers. For instance, if $P(\mathbf{r})$ is independent of \mathbf{r} , corresponding to random stacking, $s=0$ and $F=1$.

Since an inspection of Fig. 4 suggests that there are interlayer stacking correlations in our sample, we have parametrized our data using the simplest model that includes such correlations. Within this model, if a particular layer is said to occupy position A , then the next layer has probability p of being shifted or rotated by a random amount, while the probabilities of occupying positions B and C are both equal to $(1-p)/2$; longer-range correlations are neglected. Hence,

$$P(\mathbf{r}) = \frac{2}{ab} p + [\delta(\mathbf{r}-\mathbf{r}_B) + \delta(\mathbf{r}-\mathbf{r}_C)] \frac{1-p}{2}, \quad (4)$$

where $ab/2$ is the area of the unit cell, and $\mathbf{r}_B(\mathbf{r}_C)$ is the in-plane component of the offset of the $B(C)$ position from the A position.

The calculated intensity was modified to reflect variations in the effective scattering volume with Q , and the effects of sample container absorption. Due to the small sample volume and small sample absorption coefficient, absorption by the sample itself was negligible. Thus the hk profile can be described with only four adjustable parameters: (i) a constant background, (ii) an overall scale factor, (iii) the probability that a pair of adjacent layers is randomly aligned (p), and (iv) the characteristic dimension of a planar domain (D).

The best fit combining $00l$ and hk reflections is shown as the smooth line in Fig. 4, while the data are shown as the noisy line. From our fit we find that the probability of graphitic stacking, $(1-p)$, is $\sim 18\%$. Differences between the calculation and the experimental curve are due to uncertainties in the background and in the sample container thickness, and also due to the simplicity of the model, i.e., the neglect of variations in p among different particles, non-nearest-neighbor correlations, etc. In fact the small bump in the 10 peak line shape, not described by the model, suggests that $(1-p)$ is larger than 18% for many of the particles in our sample. The existence of interlayer correlations is an important finding, because it places constraints on the microstructure of the nanotubes and nanoparticles. Such correlations tend to reduce the interlayer interaction energy, which plays an important role in the formation of nanotubes and nanoparticles.

The inset to Fig. 4 shows the results of a high-resolution measurement in the region around the 10 two-dimensional reflection. The line shape in this region is sensitive to the size of the average coherent planar

domain. Best agreement of the theoretical curve with the data was obtained with $D = 400 \pm 30 \text{ \AA}$.

IV. THEORETICAL RESULTS

In Sec. III we modeled the diffraction from a stack of partially ordered graphite sheets and obtained very good agreement with the experimental data when $\sim 18\%$ of adjacent layer pairs were ordered as in crystalline graphite. In this section we address the possibility that interlayer correlations occur in nanotubes and nanoparticles, where sheet curvature and geometrical restrictions impose constraints on interlayer ordering. We also examine the influence of nanotube curvature on the finite size broadening of hk peaks.

We start with an introduction to relevant notation and definitions. We then discuss aspects of the geometry of nanotubes in the large diameter approximation, and their implications regarding the extent to which adjacent layers can be correlated. Finally we present the results of computer calculations for nanotubes without invoking this approximation.

A. Axial, nonaxial, and $00l$ reflections

The long axis of a nanotube is called the z axis, and at any location on a nanotube the radial direction is the c direction (to make correspondence with graphite), and the tangential direction is the ϕ direction (Figs. 1 and 2).

To discuss the periodic atomic arrangements that are responsible for coherent reflections, let us first consider single-layer nonhelical nanotubes (Fig. 2). Atoms in such tubes sit on rings that are periodically arranged along the z axis. The repeat period T of the z coordinates is $a/2$ for $\theta=0^\circ$ nanotubes and $b/2$ for $\theta=30^\circ$ nanotubes. Nonhelical nanotubes contain regions that scatter x rays coherently for any wave vector \mathbf{q} whose z component is $q_z = 2\pi n/T$ where n is an integer. These reflections will be called axial hk reflections.

In addition to translational periodicity along the z axis, the atomic positions in nonhelical nanotubes have angular and helical periodicities, the latter involving a rotation followed by a translation along the z axis. These lead to approximate local in-plane translational periodicities resulting in coherent scattering with two-dimensional Miller indices hk as in graphite. These will be called nonaxial hk reflections.

Axial and nonaxial reflections from an approximately flat local region of a $\theta=0^\circ$ nanotube are illustrated in Fig. 7. The powder peak labeled 11 is due to the six distinct reflections 11 , $\bar{1}1$, $1\bar{2}$, $\bar{1}\bar{2}$, $2\bar{1}$, and $\bar{2}1$. In $\theta=0^\circ$ nanotubes two of these six reflections are axial, but there are no axial reflections of this type in $\theta=30^\circ$ nanotubes. Similarly the 10 powder peak is due to the six distinct reflections 10 , $\bar{1}0$, 01 , $0\bar{1}$, $\bar{1}1$, and $1\bar{1}$, two of which are axial in $\theta=30^\circ$ nanotubes, while in this case there are no axial reflections in $\theta=0^\circ$ nanotubes. In helical nanotubes all of the 10 and 11 reflections are nonaxial.

Helical nanotubes are also periodic in the z direction but with T much greater than a or b . Our calculations confirm that the structure factors for the axial reflections are negligibly small, and they will be ignored in the rest

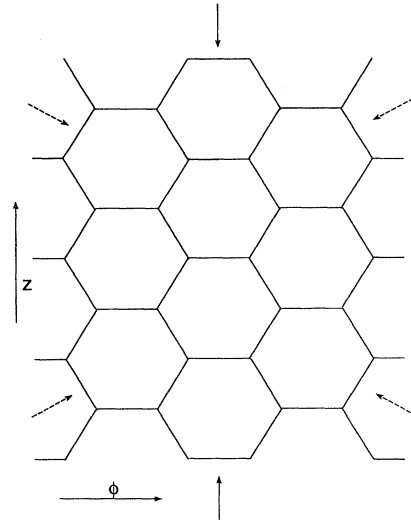


FIG. 7. A small region of a large diameter nonhelical $\theta=0^\circ$ nanotube (cf. Fig. 2). Arrows represent directions of in-plane components of \mathbf{q} for 11 reflections: solid—axial; dashed—nonaxial. In all cases the magnitudes of the in-plane components of \mathbf{q} are $4\pi/a$, and the out-of-plane components of \mathbf{q} (in the radial c direction) are arbitrary.

of the paper. Within this approximation coherent scattering in helical nanotubes results exclusively from the helical periodicity of the atomic positions, and helical nanotubes have exclusively nonaxial reflections.

Analytical and numerical calculations¹⁷ show that both axial and nonaxial hk reflections in single-wall nanotubes produce characteristic two-dimensional sawtooth powder line shapes, originally calculated for graphite by Warren.¹³ Preferred stacking of adjacent layers in multilayer nanotubes can modulate the tails of these reflections.

Radial periodicity in multilayer nanotubes results in approximate translational periodicity in the stacking (radial) direction in each local region. Reflections due to this periodicity appear at $Q = \pi l/d_c$, where l is even, and will be called $00l$ reflections. In the powder pattern they appear as symmetric peaks.

B. Large diameter approximation

The purpose of this section is to develop a basic understanding of the constraints placed on interlayer correlations and finite-size broadening effects due to the simple fact that nanotubes are made of graphite sheets rolled into cylinders, imposing a boundary condition that is absent in flat graphite. We will consider large diameter nanotubes, in which there are many carbon atoms on the circumference of a given layer. It is then sufficient to investigate the statistical distribution of stacking arrangements in order to determine whether or not the hk reflections are modulated by interlayer correlations. To examine stacking in nonhelical nanotubes, consider Fig. 8, which shows a projection of the positions of atoms in two adjacent layers of a $\theta=30^\circ$ nanotube onto a plane perpendicular to z . Note that the angular offsets differ at different angular positions. In fact, the ϕ offset changes

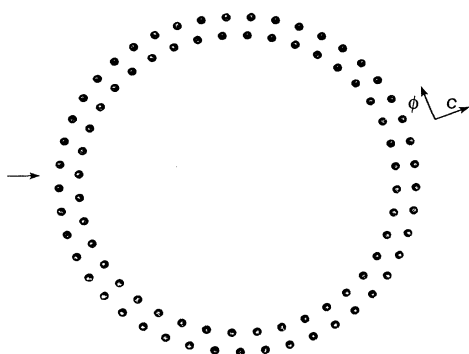


FIG. 8. Two concentric rings of atoms equally spaced in the ϕ direction. The arrow represents a region of AB graphitic alignment.

linearly with ϕ , covering the entire domain of possible offsets with essentially equal probability as long as the diameter is “large.” Thus in a powder-diffraction experiment, the sampled distribution of offsets is random and nonaxial hk reflections cannot be modulated. The same argument applies to $\theta=30^\circ$ scroll nanotubes and to $\theta=0^\circ$ nanotubes of both types. Helical nanotubes have additional disorder along the z axis and cannot have modulated hk reflections. Nanoparticles consisting of nearly spherical fullerene-like concentric shells cannot have modulated hk reflections for analogous reasons.

Axial hk reflections in nonhelical nanotubes are insensitive to ϕ offsets, because they have no component of \mathbf{q} parallel to ϕ (Fig. 7). These reflections can therefore be modulated if there is preferential alignment of layers in the z direction. In nonhelical scroll tubes all layers have the same z axis coordinates, and the axial hk reflections are modulated. On the other hand, any stacking is allowed in Russian doll tubes and the axial hk reflections are modulated if adjacent layers are not randomly stacked along the z axis. Calculations are required to determine the energetically favorable stacking arrangements.

Another important consequence of the curvature of nanotubes is that the coherently diffracting domain is confined to a small region unless \mathbf{q} is parallel to \mathbf{z} . The size of the coherent domain for a nonaxial hk reflection is equal to $A/\sin(\chi_{hk})$ where A is a function of the tube radius and χ_{hk} is the angle between the translational periodicity vector for the hk reflection and \mathbf{z} . On the other hand the finite size of the coherent domains for axial reflections is proportional to the length of the tube.

$$I(Q) = \frac{C(Q)f^2(Q)}{Q^2} \text{Av} \left[\frac{2\pi}{L} \sum_{q_z < Q} \int_0^{\sqrt{Q^2 - q_z^2}} \delta(q_c - \sqrt{Q^2 - q_z^2}) \sum_{i,i'} e^{i\mathbf{q} \cdot (\mathbf{r}_i - \mathbf{r}_{i'})} q_c dq_c \right], \quad (7)$$

where L is the length of the tube, and q_c is the radial component of \mathbf{q} .

Calculations were performed for Russian doll and scroll types of nanotubes. Equation (7) was evaluated by

Thus we expect the finite-size broadening of the axial reflections to be much smaller than that of the nonaxial reflections, since the tube length is much greater than its radius. An exact analytic calculation and quantitative discussion of the finite-size broadening of hk peaks will be given in a separate paper.¹⁷

C. Beyond the large diameter approximation

In order to determine whether or not the diameters of the nanotubes in our sample are sufficiently large that the large diameter approximation is justified, we have performed numerical calculations of powder-diffraction patterns of nanotube samples with layers of the same helicity. For x-ray-scattering measurements the diffracted intensity is proportional to

$$I(Q) = \frac{C(Q)f^2(Q)}{Q^2} \int d\mathbf{q} \delta(|\mathbf{q}| - Q) G(\mathbf{q}), \quad (5)$$

where the ensemble averaged structure factor

$$G(\mathbf{q}) = \text{Av} \left[\sum_{i,i'} e^{i\mathbf{q} \cdot (\mathbf{r}_i - \mathbf{r}_{i'})} \right]. \quad (6)$$

Here \mathbf{r}_i is the position of atom i , Av represents the ensemble average, $1/Q^2$ is the Lorentz factor, and $C(Q)$ and $f(Q)$ are the polarization factor and atomic scattering factor, respectively. Nanotube curvature complicates the exact analytic evaluation of Eq. (5) and such calculations will be described in a separate paper.¹⁷ Here we will present the results of numerical calculations and discuss the main features of $G(\mathbf{q})$ (see also Ref. 14).

Because of translational periodicity along the z axis, $G(\mathbf{q})$ is nonzero only at discrete values of q_z (assuming infinite length tubes). The relevant q_z values in nonhelical tubes are integer multiples of $2\pi/a$ for $\theta=0^\circ$ tubes and of $2\pi/b$ for $\theta=30^\circ$ tubes. In our calculations for helical nanotubes we only sum over the reciprocal space sheets that contribute significantly to the hk peaks. The q_z values of these sheets can be calculated explicitly; q_z values contributing to the 10 peak are $(4\pi/b)\sin(\pi/6 + n\pi/3 + \theta)$ and q_z values contributing to the 11 peak are $(4\pi/a)\sin(n\pi/3 + \theta)$, where n is any integer.

Since the ensemble averaged reciprocal-space density $G(\mathbf{q})$ has cylindrical symmetry, and since q_z is restricted to a set of specific values, we can reduce the three-dimensional integral in Eq. (5) to a finite sum over one-dimensional integrals:

generating the coordinates of the atoms of a nanotube of finite length, calculating the values of q_z that contribute to the sum, and then evaluating the integral numerically. Ensemble averages were performed by summing over

contributions from 300 nanotubes of a given type and helicity with specified rectangular distributions of inner diameters and lengths. Additional parameters for ensembles of Russian doll tubes were an interlayer correlation parameter and the distribution of the number of layers. The stacking model for the Russian doll tubes was analogous to the model described in Sec. III: adjacent layers were assumed to be randomly aligned with probability g and otherwise a randomly picked pair of unit cells in adjacent layers was aligned as in graphite. Additional parameters for scroll tubes were the density of dislocation defects and the average length of the spiral; dislocations were modeled as random translations in the z and "spiral" directions. The structural parameters of each nanotube, such as the number of layers, and the locations of defects, were randomly generated within the specified distributions.

In Fig. 9(a) we show a calculated diffraction pattern for an ensemble of nonhelical Russian doll nanotubes with helical angle $\theta=0^\circ$ and randomly stacked layers ($g=1$); Fig. 9(b) shows a calculation for $\theta=0^\circ$ scroll tubes with an average of ~ 5 dislocation defects per tube. Both structures had inner diameters of 20–40 Å, 5–21 layers, and 200–300 unit cells along the z axis. The diffraction pattern in Fig. 9(a) is also characteristic of all helical nanotubes and the pattern in Fig. 9(b) is characteristic of $\theta=0^\circ$ Russian doll tubes with interlayer correlations along the z axis. The 10 peak contains no axial reflections in these nanotubes and is therefore not modulated. Its line shape is in excellent agreement with the line shape calculated for disordered graphite [Eq. (3)] with $p=1$. Two of the six reflections in the 11 peak are axial, so they are modulated in tubes with correlations

along the z axis, resulting in the extra peaks seen in Fig. 9(b). They are equivalent to the 112 and 114 peaks in graphite.

We have also investigated the dependence of the 11 peak line shape on the degree of z axis ordering, by performing the same calculation with a high density of Q points for $\theta=0^\circ$ Russian doll nanotubes (Fig. 10); the structural parameters were the same as in the previous calculation, and the probability of random alignment (g) was 1, 0.55, and 0 for the bottom, middle, and top curves, respectively.

The bottom curve exhibits asymmetric peaks with maxima at $\sim 5.13 \text{ \AA}^{-1}$ and at $\sim 5.2 \text{ \AA}^{-1}$, both having broad tails on the high- Q side characteristic of two-dimensional reflections, as well as a broad peak at $\sim 5.57 \text{ \AA}^{-1}$. Our analysis reveals that the $\sim 5.13 \text{ \AA}^{-1}$ peak is due to the axial 11 reflections (we call it the axial 11 peak), the $\sim 5.2 \text{ \AA}^{-1}$ peak results from the nonaxial 11 reflections (we call it the nonaxial 11 peak), and the peak at $\sim 5.57 \text{ \AA}^{-1}$ is the 006 reflection. The nonaxial 11 peak has a maximum at higher Q and is much broader than the axial 11 peak because, as discussed in Sec. IV B, curvature limits the coherently diffracting domain for the nonaxial peak; this results in finite-size broadening and a shift of its maximum.^{10,13} From the shift of the maximum we estimate that the 11 nonaxial reflection coherent domain size is $\sim 60 \text{ \AA}$. As predicted in the large diameter approximation, ordering of layers along the z direction introduces modulations into the axial 11 peak, evidenced as the broad bump at $\sim 5.4 \text{ \AA}^{-1}$ in the middle curve of Fig. 10 ($g=0.55$), and as sharp symmetric 11/ peaks in the top curve ($g=0$). Note too that much of the axial 11 peak sharpens into a symmetric 110 peak as g is decreased from 1 to 0. On the other hand interlayer ordering does not affect the nonaxial 11 peak.

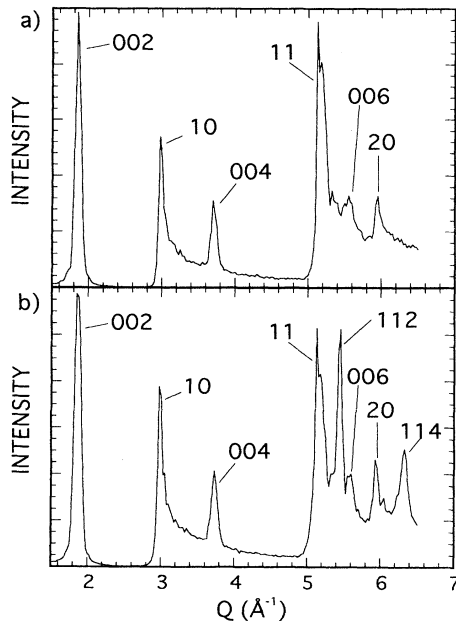


FIG. 9. A calculation of the diffraction pattern for $\theta=0^\circ$ nonhelical nanotubes: (a) Russian doll tubes with no z -axis interlayer correlations. (b) Scroll tubes with dislocations.

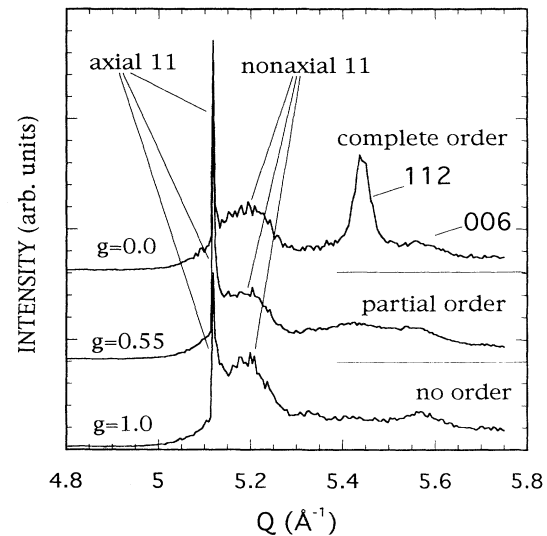


FIG. 10. A calculation of the diffraction pattern for $\theta=0^\circ$ nonhelical Russian doll nanotubes with different z -axis interlayer correlation parameters g (defined in the text). The diffraction pattern below 4.9 \AA^{-1} is not affected by interlayer ordering.

No splitting of hk peaks into axial and nonaxial components, such as is shown in Fig. 10, has yet been observed experimentally, no doubt because peak line shapes are strongly smeared owing to variations of helicity in available samples. A more detailed theoretical investigation of finite-size effects in nanotubes is currently underway.¹⁷

V. DISCUSSION AND CONCLUSIONS

In Sec. IV we showed that the curvature of the graphitic layers in nanotubes precludes the possibility of interlayer stacking correlations unless the tubes are nonhelical. We also found that a sample consisting of $\theta=0^\circ$ nonhelical nanotubes has an unmodulated 10 peak and a 11 peak with modulated and unmodulated components whose integrated intensity ratio is 1:2 (Fig. 10); conversely a sample of $\theta=30^\circ$ nonhelical nanotubes has an unmodulated 11 peak and a 10 peak whose modulated and unmodulated component intensities are again in the ratio 1:2. This is because none of the six 10 (11) reflections and only two of the six 11 (10) reflections in $\theta=0^\circ$ ($\theta=30^\circ$) nanotubes are axial, and the axial reflections are modulated whereas the nonaxial reflections are not. In an attempt to interpret our data within the theoretical framework developed in Sec. IV, and in a manner consistent with our TEM results, we shall assume that 40% of the sample is spherical nanoparticles (which have no modulated reflections), and that the remaining material is exclusively nonhelical $\theta=0^\circ$ and $\theta=30^\circ$ nanotubes. The two types of nonhelical nanotubes are assumed to be present in roughly equal proportions since the observed 10 and 11 reflections are both modulated. This picture, which maximizes the modulated component in the hk peaks, implies that the integrated intensities of the modulated components of the 10 and 11 peaks amount to about 10% of the total integrated intensity.

We have so far assumed that the fraction of fully nonhelical nanotubes is 100%. However, recent TEM studies^{8,18} have shown that this fraction is actually much smaller. Furthermore the measured distribution of interlayer d spacings in our sample (Fig. 6) is completely inconsistent with the bimodal distribution expected for a sample which consists of nothing but nonhelical nanotubes in equal proportions; $\theta=0^\circ$ and $\theta=30^\circ$ Russian doll nanotubes have interlayer d spacings of ~ 3.39 and ~ 3.52 Å, respectively. The preponderance of helical nanotubes in our sample means that the modulated component of the hk reflections should be much less than 10% so that interlayer correlations are very unlikely to be observable in experimental measurements if the model assumed in Sec. IV is correct.

Since we do observe modulated hk peaks, and since our sample is largely nanotubes, we are forced to conclude that our idealized structural models of nanotubes are incorrect. On the other hand, we showed in Sec. III that

our data are well described by a model of disordered graphite in which the probability of graphitic stacking is 18%. This suggests that the observed interlayer correlations may arise from flat domains which locally approximate graphite. It is clear from Figs. 1 and 8 that nanotubes of the same helicity contain regions where the alignment of atoms in adjacent layers is close to that of graphite, and others where it is not. Zhang *et al.*⁸ proposed that the interlayer stacking energy would be optimized if flattened regions approximating graphitic alignment were created at the expense of additional curvature in other regions, resulting in nanotubes and nanoparticles with polygonal cross sections. Polygonal nanotubes and nanoparticles would also have different interlayer spacings in the bent and flat regions.¹⁸ Thus polygonization would naturally explain both the existence of interlayer correlations and the broad distribution of interlayer spacings observed in our experiment. Polygonal nanotubes and nanoparticles have already been observed with high-resolution TEM (HRTEM).^{8,18} Furthermore Liu and Cowley¹⁸ have observed hkl spots in diffraction profiles of individual nanotubes, indicating the presence of significant interlayer stacking correlations. A possible origin of polygonization¹⁹ is that it is due to sp^3 defect structures.

It is tempting to think that the modulated hk reflections are exclusively due to polygonal nanoparticles, since TEM measurements clearly show that many of them are faceted. In this case, since our sample is 40% nanoparticles, we expect at most 40% intensity to be modulated and the data should be well described by a fit to a component with $p=0$ and 60% of the integrated intensity and a second component with $p\neq 0$ and 40% of the integrated intensity. However, the one component fit described in Sec. III gave a much better description of the data, implying that interlayer correlations are present in both tubes and particles in our sample.

We have observed short-range graphitic interlayer stacking correlations in the diffraction pattern of a carbon nanotube/nanoparticle sample. We have also performed calculations which show that such correlations should not be observable, given what is known about the helicities of nanotubes, unless we assume, consistent with recent HRTEM observations, that the carbon atoms in nanotube/nanoparticle samples largely condense into flat regions with graphitelike interlayer correlations. This suggests that carbon nanomaterial is mostly polygonal. However, the present x-ray-diffraction measurements cannot distinguish between Russian doll and scroll tubes, nor can they determine whether the flat domains are connected by regions of continuous curvature or by the highly disordered regions proposed by Zhou *et al.*⁵

ACKNOWLEDGMENT

D.R. was supported by the National Research Council.

- ¹S. Iijima, *Nature (London)* **354**, 56 (1991).
- ²P. J. F. Harris, M. L. H. Green, and S. C. Tsang, *J. Chem. Soc. Faraday Trans.* **89**, 1189 (1993).
- ³S. Iijima and T. Ichihashi, *Nature (London)* **363**, 603 (1993); D. S. Bethune, C. H. Kiang, M. S. deVries, G. Gorman, R. Savo, J. Vazques, and R. Beyers, *ibid.* **363**, 605 (1993).
- ⁴S. Iijima, T. Ichihashi, and Y. Ando, *Nature (London)* **356**, 776 (1992); M. Ge and K. Sattler, *Science* **260**, 515 (1993).
- ⁵O. Zhou, R. M. Fleming, D. W. Murphy, C. H. Chen, R. C. Haddon, A. P. Ramirez, and S. H. Glarum, *Science* **263**, 1744 (1994).
- ⁶C. T. White, D. H. Robertson, and J. Mintmire, *Phys. Rev. B* **47**, 5485 (1993).
- ⁷M. S. Dresselhaus, G. Dresselhaus, and S. Saito, *Phys. Rev. B* **45**, 6234 (1992).
- ⁸X. F. Zhang, X. B. Zhang, G. Van Tendeloo, S. Amelinckx, M. Op de Beeck, and J. Van Landuyt, *J. Cryst. Growth* **130**, 368 (1993).
- ⁹T. W. Ebbesen and P. M. Ajayan, *Nature (London)* **658**, 220 (1992).
- ¹⁰Y. Saito, T. Yoshikawa, S. Bandow, M. Tomita, and T. Hayashi, *Phys. Rev. B* **48**, 1907 (1993).
- ¹¹A. Guinier, *X-ray Diffraction in Crystals, Imperfect Crystals, and Amorphous Bodies* (Freeman, San Francisco, 1963).
- ¹²M. A. Krivoglaz, *Theory of X-ray and Thermal Neutron Scattering by Real Crystals* (Plenum, New York, 1969).
- ¹³B. E. Warren, *Phys. Rev.* **59**, 693 (1941).
- ¹⁴H. Shi, J. N. Reimers, and J. R. Dahn, *J. Appl. Crystallogr.* **26**, 827 (1993).
- ¹⁵V. A. Drits and C. Tchoubar, *X-ray Diffraction by Disordered Lamellar Structures* (Springer-Verlag, New York, 1991).
- ¹⁶P. W. Stephens, P. A. Heiney, R. J. Birgeneau, P. M. Horn, D. E. Moncton, and G. S. Brown, *Phys. Rev. B* **29**, 3512 (1984).
- ¹⁷D. Reznik (unpublished).
- ¹⁸M. Liu and J. M. Cowley, *Ultramicroscopy* **53**, 333 (1994).
- ¹⁹H. Hiura, T. W. Ebbesen, J. Fujita, K. Tanigaki, and T. Tanada, *Nature (London)* **367**, 148 (1994).

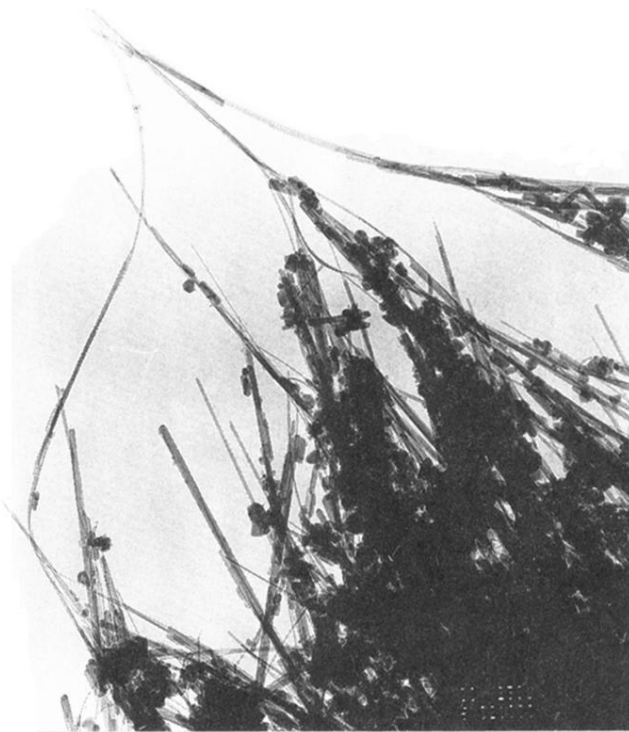


FIG. 3. Low resolution TEM photograph of a part of the sample used in our measurements. The area shown is approximately $36 \times 46 \mu\text{m}^2$.